A Ground Fault Location and Severity Estimation Method for Modular Multilevel Converters

José M. Guerrero, *Member, IEEE,* Aitor Blázquez-Campanón, Salvatore D'Arco, Miguel Jiménez Carrizosa, Kumar Mahtani and Carlos A. Platero, *Senior Member, IEEE*

***Abstract*—The need of efficient electric transmission systems, the rise of renewable energy production and battery storage systems has empowered the use of Modular Multilevel Converters (MMC) which allows a better performance than convenctional converters. However, the diagnosis of electrical faults in MMC is more challenging because more components are involved in the fault circuit. Particularly, ground faults (GF) are the most common type of faults in power systems and their diagnosis has not been widely studied for AC-DC converters, where most of the industrial relays fail. This paper proposes a GF location method for MMC based on a high value grounding resistor placed in its DC midpoint or AC neutral point. Measuring the voltage between its terminals, and performing its frequency analysis, the fault can be located. The novelty of this method resides in the location of the GF in the AC side, DC side or in a faulty submodule (SM) of the MMC. Numerous simulations were performed in a half-bridge three-phase MMC converter obtaining promising results. Afterwards, experimental tests in a 60 kVA 12-levels three-phases MMC were carried out, validating the method. The errors achieved are lower than 2 SM for fault resistances up to 11 kΩ.**

***Index Terms*— Electrical fault detection, Fault current limiters, Fault location, Frequency response, Multilevel converters, Voltage measurement.**

NOMENCLATURE

C	Capacity
f_0	DC component
f_1	Fundamental frequency
i	Number of the phase
I_f	Fault current
j	Number of submodule
K	Attenuation factor
L_{filter}	Inductive filter
N	Total number of submodules per arm
R_1, R_2	Artificial midpoint resistances
R_f	Fault resistance
R_{gnd}	Grounding resistor
t	Time
T	Period
U_C	Capacitor voltage
U_{DC}	Total DC voltage
uf	Instantaneous voltage in the fault resistance
U_f	Voltage in the fault resistance
U_{gnd}	Grounding resistor voltage
u_{gnd}	Instantaneous grounding resistor voltage
U_{in}	AC *i-th*-phase voltage
u_{in}	Instantaneous AC phase voltage
U_{Li}	Lower arm voltage of the *i-th* phase
U_{Li1}	Lower arm voltage of the *i-th* phase above the fault position
U_{Li2}	Lower arm voltage of the *i-th* phase below the fault position
U_{SMj}	Voltage in the *j-th* submodule
U_{Ui}	Upper arm voltage of the *i-th* phase
U_x	Voltage in the fault position
x	Fault position
X	Submodule in fault
α	Stopping conduction angle
β	Starting conduction angle
ω	Electric pulsation

This research has been performed using the ERIGrid 2.0 Research Infrastructure and is part of a project (DIAPROCON) that has received funding from the European Union's Horizon 2020 Research and Innovation Programme under the Grant Agreement No. 870620. The support of the European Research Infrastructure ERIGrid 2.0 and its partner SINTEF Energi AS is very much appreciated. Furthermore, this work was supported in part by the Basque Government and GISEL research group (Universidad del País Vasco) under grant OT1522-22 and in part by the European Union-Next Generation EU under grant "INVESTIGO".

Jose M. Guerrero and Aitor Blázquez are with the Department of Electrical Engineering of the Universidad del País Vasco/Euskal Herriko Unibertsitatea (UPV/EHU), 48940 Leioa, Spain (e-mails: josemanuel.guerrerog@ehu.eus and aitor.blazquez@ehu.eus).

Salvatore D'Arco is with the Department of Energy Systems of SINTEF Energy Research, 7034, Trondheim, Norway (e-mail: salvatore.darco@sintef.no).

Miguel Jimenez Carrizosa is with the Energy and Fuels Department of the Universidad Politécnica de Madrid, 28003, Madrid, Spain (e-mail: miguel.jimenezcarrizosa@upm.es).

Kumar Mahtani and Carlos A. Platero are with the Automatic, Electric and Electronic Engineering and Industrial Computing Department of the Universidad Politécnica de Madrid, 28003, Madrid, Spain (e-mails: kumar.mahtani@upm.es, carlosantonio.platero@upm.es).

I. INTRODUCTION

THE use of Modular Multilevel Converters (MMC) is nowadays widespread in power system applications such as in High Voltage Direct Current (HVDC) transmission links [1], battery energy storage systems [2], STATCOM [3] or wind renewable energy integration [4] among others due to their high performance in terms of AC current harmonic components and DC voltage modulations.

MMCs are composed of submodules (SM) where a capacitor is placed with power electronic elements, such as IGBTs. Depending on the SM topology, different strategies of switching IGBTs will charge and discharge the capacitors

according to system requirements [5]. The more submodules the MMC has, the smoother the voltages and currents waveforms are.

However, one of the difficulties that MMCs present is the fault location against electric faults due to their big quantity of elements [6]. Most of conventional relays are prepared to protect AC or DC sides of a converter but not both of them. When relays are operating in converter-based systems, commutation noises or the appearance of DC components in AC relays, which can saturate the current transformers, are common problems of these protections [7].

This paper is focused on ground faults (GFs), which are the most probable type of faults in power systems, and they are given mostly due to insulation degradation [8] between a conductor and ground. In ungrounded or high impedance grounding systems, a first fault does not provoke any damages as there is not returning path for the fault current, but if a second one occurs, the damages will be irreversible [9].

In this research area, a lot of studies have been carried out for electrical machines [10], microgrids [11], transmission lines [1], solar photovoltaics [12], etc. In MMCs, GFs can appear at both sides of the converter. For the DC side of the converter, traveling waves and artificial intelligence techniques can be used for the fault location [1], but other methods such as active AC current or voltage injection in the DC system can be also implemented to achieve the same purposes [13]. If the system is ungrounded, for DC fault location, some methods wait to a phase-to-phase short circuit to activate the DC overcurrent relays instead of locating the first GF [14]. In case of having GFs in the AC side, some methods propose the AC voltage monitoring and tripping when a voltage sag appears accompanied by an instantaneous power reduction [14]. In [15], the authors propose utilizing the positive- negative- and zero-sequences to report GFs in the AC side or in the DC side of the MMC. Other possible techniques are based on overvoltage, power ripples and zero-sequence voltage components during GFs if the MMC is ungrounded [16]-[17]. Other methods are based on the faulty SM capacitor overvoltage and zero sequence current measurements to detect faults in the power transformer AC side of the MMC [18]-[19]. However, these methods can be used only if the DC midpoint is rigidly grounded, i.e., in bipolar configurations. Furthermore, they require a lot of voltage measurements that are not commonly available in industrial MMC facilities. Finally, GFs can appear in the SM of the MMC. As far as it is known, no information about detection techniques for SM of MMCs has been found.

In order to protect both sides of a power converter, authors previous developed a detection method able to discern between DC side faults and AC side faults in electric vehicles by high resistive impedance grounding the DC midpoint of the DC side [20]. An extension of the method for grid-connected variable speed drives was also studied in [9], placing the grounding resistor in the neutral of the main power transformer that fed the drive. With this method, the power converter discerning in case of a back-to-back configuration is possible. However, both methods were applied directly to six-pulse IGBTs power converters; consequently, it was not able to locate the SM with GF.

In this paper, a GF detection and location method is proposed for MMCs. The method is also based on a high value grounding resistor placed on the neutral of the AC side of the MMC or in the midpoint of the DC side of it. In any case, the voltage is measured between the grounding resistor terminals and analyzing its frequency spectrum, the GF can be located in the AC side, in the DC side or in the faulty SM inside the converter. The method was briefly presented in a conference [21] and it also granted a Spanish Patent [22]. In this manuscript, the experimental validation of the method and a deeper theoretical understanding are presented.

The main advantages of the method are:

- The current is limited through a high value grounding resistor, then, the fault location can be done in steady state allowing the healthy operation of the MMC.
- Only three voltage measurements (AC voltage, DC voltage and grounding resistor voltage) are needed to estimate the GF parameters in terms of position and fault resistance.

The paper is structured as follows: Section II describes the operation principles of the proposed GF location method. Then, Section III describes the simulation setup and analyze different GF results. Finally, Section IV concludes the paper summing up the main ideas of the manuscript.

II. Methodology

This section describes the operation principles of the proposed method. In Fig. 1, a typical configuration of a half-bridge (HF) or full-bridge (FB) three-phase monopole MMC is shown for two different grounding types, but other many configurations of SM could be adopted. In Fig. 1.a, a high value grounding resistor, R_{gnd}, has been placed in the AC neutral of the secondary of the main power transformer. It limits the fault current. Also, the voltage is measured between its terminals, U_{gnd}. As the fault current is limited to low values, it is not necessary to actuate in a very short period of time allowing the steady-state observation of the fault and not requiring high computational costs or low response time. In case of not having access to this point, Fig. 1.b shows an alternative connection to an artificial midpoint (an artificial neutral point in the AC side could also be used).

In order to explain the operation principles of the location method with the greatest simplicity possible, a HF-MMC case study will be used with a DC midpoint grounding.

A. Expected voltage in the grounding resistor attending to the fault position

From Fig. 2.a, the healthy state relationship between the DC voltage, upper and lower arm voltages and AC voltage of the *i-th* phase can be stated as:

$$u_{Ui} = \frac{U_{DC}}{2} - u_{in} \quad (1)$$

$$u_{Li} = \frac{U_{DC}}{2} + u_{in} \quad (2)$$

Afterwards, a fault case can be analyzed. In Fig. 2.b, an example for a lower arm fault is plotted. However, different

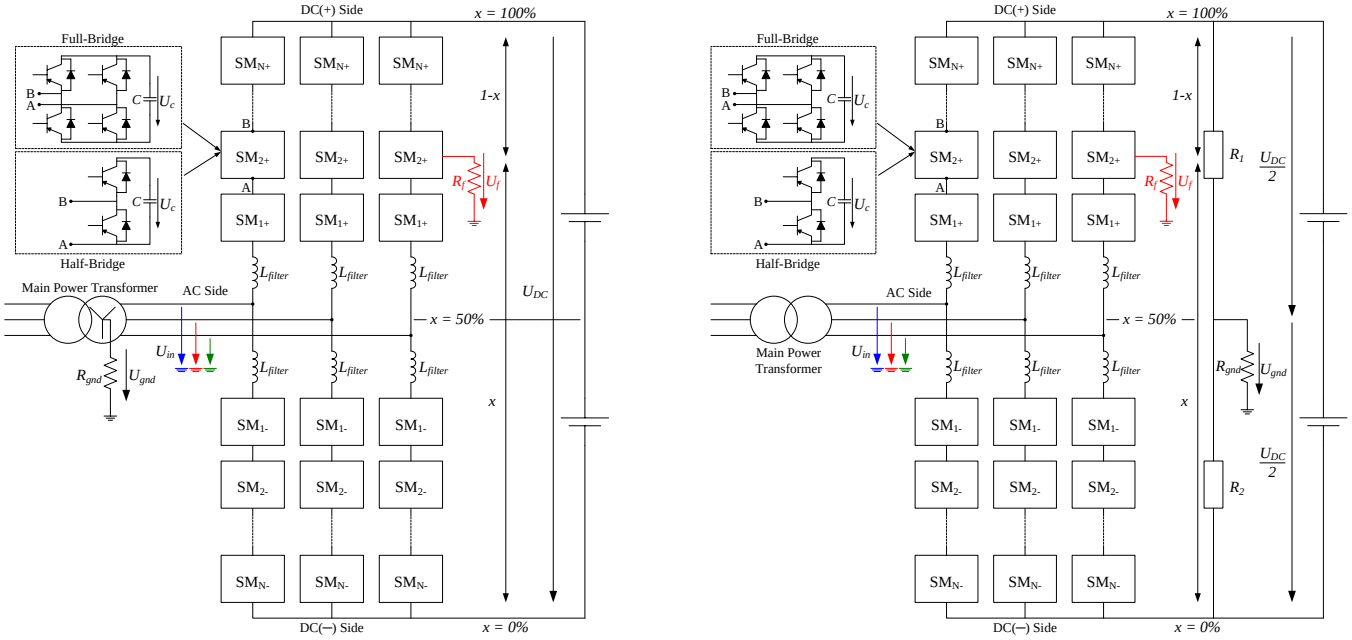

Fig. 1. Proposed grounding resistor emplacement and system analysis with a GF in a submodule [(a): grounding resistor placed in the AC neutral; (b): grounding resistor placed in a DC artificial midpoint ($R_1 = R_2$)].

fault locations can be studied. Beforehand, the extreme faults are analyzed, i.e., DC positive pole, DC negative pole and AC side. The second Kirchhoff law is applied to the fault circuits obtaining the expressions (3) to (5), respectively:

$$\frac{U_{DC}}{2} + u_{gnd} - u_f = 0 \tag{3}$$

$$\frac{U_{DC}}{2} - u_{Li} - u_{Ui} + u_f - u_{gnd} = 0 \tag{4}$$

$$\frac{U_{DC}}{2} - u_{Ui} + u_{gnd} - u_f = 0 \tag{5}$$

From (1) and (2) it can be stated that:

$$U_{DC} = u_{Li} + u_{Ui} \tag{6}$$

Additionally, the fault current, I_f, that flows through R_f is the same that circulates through R_{gnd}, then:

$$I_f = -\frac{U_{gnd}}{R_{gnd}} = \frac{U_f}{R_f} \tag{7}$$

If the system is healthy, i.e., GF does not exist, U_{gnd} will be null as there is no fault current. However, once the GF fault happens it can occur in three different zones. Consequently, applying the corresponding equations (6) and (7) into (3),(4) and (5), the final expressions (8) to (10) are obtained, respectively:

$$U_{gnd} = \frac{-U_{DC}/2}{(1 + R_f/R_{gnd})} \quad ; \quad x = 100\% \tag{8}$$

$$U_{gnd} = \frac{+U_{DC}/2}{(1 + R_f/R_{gnd})} \quad ; \quad x = 0\% \tag{9}$$

$$U_{gnd} = \frac{-U_{in}}{(1 + R_f/R_{gnd})} \quad ; \quad x = 50\% \tag{10}$$

On the one hand, DC side faults can appear, which will cause a returning path from the faulty pole to R_{gnd}. The sign of U_{gnd} will have opposite polarity to the pole in fault. i.e., if a GF happens at pole (+), x = 100%, $U_{gnd}(f_0)$ will have negative value as it is stated in (8) and previously validated in [9],[20]. The analogous reasoning can be applied to the negative pole faults as seen in (9).

On the other hand, AC side GFs can happen, then U_{gnd} will acquire an AC waveform with the frequency of the grid as stated in (10). To detect it, a Fast Fourier Transform (FFT) can be done in U_{gnd} in order to extract the phasor at the grid fundamental frequency f_1. As it happened in the DC poles, eq. (10) and previous investigations corroborate that the faulty phase can be detected by comparing the first harmonic phasor phase voltage, U_{in}, with $U_{gnd}(f_1)$ phasor, where the faulty AC phase's voltage, U_{in}, will be in counterphase with U_{gnd} [23].

With the same described procedure, from the intermediate fault of Fig. 2.b, the following final expression is reached:

$$U_{gnd} = \frac{-U_{in} + U_{Li1}}{(1 + R_f/R_{gnd})} \tag{11}$$

If (11) is compared to (10), it can be noticed that in the lower arm, the effect of the SMs above the fault should have an added effect to the fault location.

By contrast, considering:

$$U_{Ui} = U_{Li1} + U_{Li2} \tag{12}$$

If the circuit is analyzed from the bottom the equivalent expression (13) is reached:

$$U_{gnd} = \frac{U_{DC}/2 - U_{Li2}}{(1 + R_f/R_{gnd})} \tag{13}$$

In an intermediate case, the GF can appear in a SM. In this case, U_{gnd} will have f_1 and f_0 components as an intermediate case between AC side and DC side. The proportion of f_1 and f_0 components in U_{gnd} will vary attending to the number of capacitors, C, that define the distribution U_{Ui1} + U_{Ui2}.

In order to define U_{Li1} and U_{Li2}, Fig. 3 shows a period of the lower arm commutation of "*N*" HF-SM considering Nearest Level Control (NLC), which considerably ease the theoretical definition of the SM waveforms [24].. This way, the voltage waves in each "*j-th*" SM can be defined as:

$$U_{SMj} = \begin{cases} 0 & ; \quad \forall t \in (\alpha_j, \beta_j) \\ U_{Cj} & ; \forall t \in (0, \alpha_j) \cup (\beta_j, 2\pi) \end{cases} \tag{14}$$

with U_{Cj} being U_{DC}/N, and considering that:

$$\alpha_j = \frac{\pi}{2} - \left(j - \frac{1}{2}\right) \cdot \frac{\pi}{N} \quad ; \quad j = 1,2,\dots,N \tag{15}$$

$$\beta_j = \frac{\pi}{2} + \left(j - \frac{1}{2}\right) \cdot \frac{\pi}{N} \quad ; \quad j = 1,2,\dots,N \tag{16}$$

In MMCs it is a common practice to have a voltage balancing control for the capacitors of each SM in order to maintain all of them in the same voltage or approximately, U_{Cj} = U_C [24]. It is possible by changing the conduction time of each capacitor attending to the period of the wave. In Fig. 3, the second and third plots correspond to the same SM voltage, but in different periods of the U_{Lj} voltage. Finally, an average model of the commutations can be assumed as a half-period conducting and a half-period by-passed (see in the fourth plot of Fig. 3) after a number of periods equal to the number of SM of the lower branch U_{Ui}. If a decomposition of this wave is performed in DC component and fundamental frequency in a Fourier Series, the following expression is reached:

$$U_{SMj} = \frac{U_{DC}}{2N} + \frac{U_{DC}}{2N} \cdot e^{j\omega t} \tag{17}$$

Despite that, NLC modulation has been chosen to explain the fault location method, other modulation techniques could be implemented without having considerable variations in the first harmonic and DC component of U_{SMj} [25].

It must be noticed that U_{Ui1} and U_{Ui2} are the addition of the SM that are above and below the fault respectively. Then:

$$U_{Li1} = \sum_{j=1}^{X} U_{SMj} \quad ; \quad U_{Li2} = \sum_{j=X+1}^{N} U_{SMj} \tag{18}$$

Introducing these equations (17) and (18) into (11) or (13) the following conclusion can be reached:

$$U_{gnd} = \frac{-\left(U_{in} - X\frac{U_{DC}}{2N}\right) \cdot e^{j\omega t} + X\frac{U_{DC}}{2N}}{(1 + R_f/R_{gnd})} \tag{19}$$

$$U_{gnd} = \frac{\left(1 - \frac{X}{N}\right)\frac{U_{DC}}{2} - X\frac{U_{DC}}{2N} \cdot e^{j\omega t}}{(1 + R_f/R_{gnd})} \tag{20}$$

From (1) and (2), if the arm voltages are balanced, the U_{in} voltage has an amplitude of U_{DC}/2. Taking it into account, in (19), a linear progression is given if the fault is changing its position. The fault will have 0% of DC component, U_{gnd} (f_0), and maximum AC component, U_{gnd} (f_1), for a fault in the AC side (X = 0), but it will decrease linearly to a fault in the *N-th* SM (X = N), where the AC component will be extinguished. Inverse reasoning can be applied in (20). Additionally, dividing the AC part of (19) per (10) or the DC part (20) per (9), it must be highlighted that the percentage of AC and/or

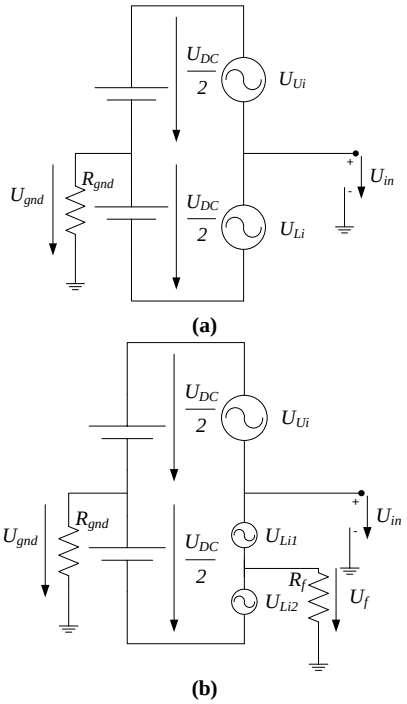

Fig. 2. Equivalent circuit of the *i-th* phase in a MMC [(a): healthy state of the MMC; (b): faulty state of the MMC with a GF in the lower arm].

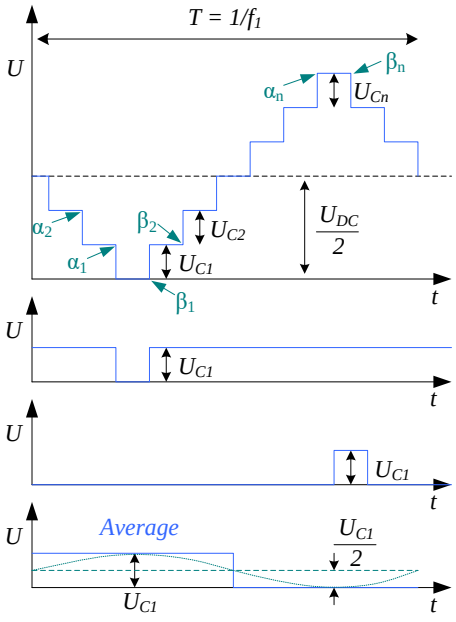

Fig. 3. From top to bottom: Lower arm theoretical waveform considering NLC; SM1 applied voltage for a determined period; SM1 voltage for another different period considering voltage balancing; SM1 average voltage.

DC reached in U_{gnd} do not depend on the R_f value. Finally, in Fig. 4, the theoretical voltage distribution along the MMC is depicted.

B. Fault location estimation

Attending to the proportion among $U_{gnd}(f_0)$ and $U_{gnd}(f_1)$ the faulty SM can be detected in percentage of arm, x, where x = 0% at the negative pole, x = 50% in the AC side and inductive filters and x = 100% in the positive pole (see Fig. 4). As $U_{gnd}(f_1)$ and $U_{gnd}(f_0)$ will decrease proportionally to the increase of R_f, the proportion among them is not affected by this fact and also the variation of these proportion are linear with x. Then, the position can be estimated with the equation shown in (21):

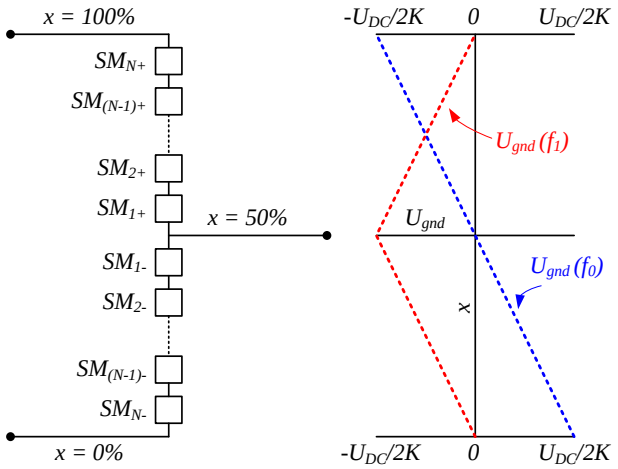

Fig. 4. U_{gnd} distribution in AC and DC component for every fault position, x, in the MMC [K is referred to the attenuation factor ($1+R_f/R_{gnd}$)].

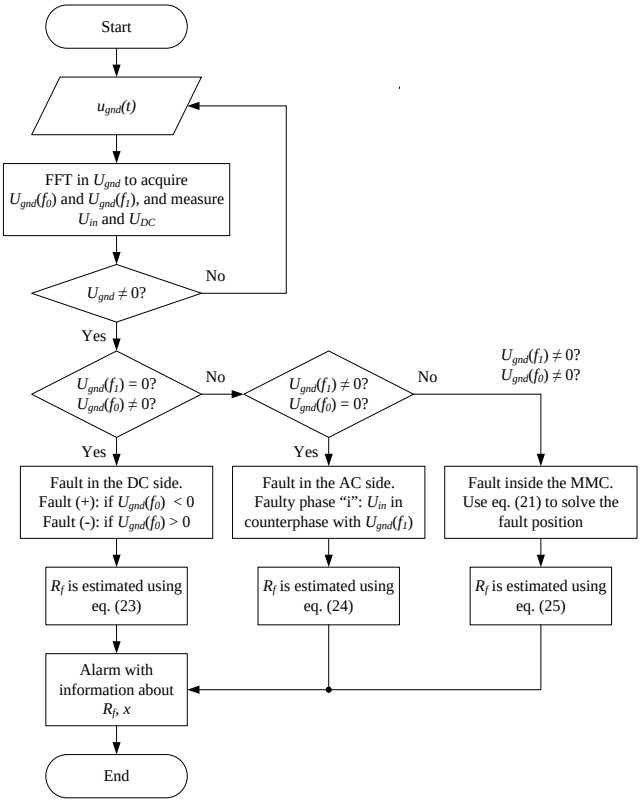

Fig. 5. Algorithm of the proposed GF location method.

$$x = \frac{1}{2} - \frac{U_{gnd}(f_0)}{2 \cdot \left(\left|U_{gnd}(f_0)\right| + U_{gnd}(f_1)\right)} \tag{21}$$

With this equation:

- In case of having faults in the AC side, $U_{gnd}(f_0)$ will be null, then x = 0.5.
- In case of fault in the DC side, $U_{gnd}(f_1)$ will be null and attending to the $U_{gnd}(f_0)$ polarity x = 0 or 1.
- In case of MMC inside faults, U_{gnd} have a DC and AC proportion that will allow the submodule position estimation.

B. Fault resistance estimation

Once the fault location is estimated, the fault resistance, R_f, can be calculated from the voltage divider between R_{gnd} and R_f in the faulty point as displayed in (22) in case of AC neutral grounding (the DC midpoint configuration must also consider R_1 or R_2 in the voltage divider):

$$U_{gnd} = \frac{R_{gnd}}{R_{gnd} + R_f} \cdot U_x \tag{22}$$

According to the next expressions extracted from (22), the fault resistance is estimated for the AC side case (23), the DC side cases (24) or the submodule cases (25), respectively:

$$R_f = -\frac{U_{in} - U_{gnd}(f_1)}{U_{gnd}(f_1)} \cdot R_{gnd} \quad ; \quad if\ x = 0.5 \tag{23}$$

$$R_f = \frac{\frac{U_{DC}}{2} - \left|U_{gnd}(f_0)\right|}{\left|U_{gnd}(f_0)\right|} \cdot R_{gnd} \quad ; \quad if\ x = 0\ or\ 1 \tag{24}$$

$$R_f = \frac{\left|\left(x - \frac{1}{2}\right) U_{DC}\right| - \left|U_{gnd}(f_0)\right|}{\left|U_{gnd}(f_0)\right|} \cdot R_{gnd} \quad ; \quad if\ x \neq 0.5 \tag{25}$$

The analogous reasoning could be performed for an artificial DC midpoint grounding obtaining equivalent equations considering also the R_1 and R_2 influence in the R_f estimation.

With this process, the method is able to locate the fault position and estimate its severity in terms of fault resistance with only three voltage measurements (the grounding resistor voltage, the AC phases voltages, and the total DC voltage). To sum up the fault diagnosis methodology, Fig. 5 displays the operation algorithm.

III. Simulations

In order to validate the method, numerous simulations have been carried out in Matlab Simulink using a monopolar three-phase MMC with HF submodules.

A. Simulation Setup

The simulation setup can be seen in Fig. 6. In this setup, the monopole three-phase MMC is composed by 10 SM per branch symmetrically divided and in HB configuration using IGBTs. Each SM has a capacitor of C = 3300 µF.

The transformer (with Yyn0 configuration) feeds the converter from the grid with U_{in} = 50 V and the DC side voltage is imposed from the other side at U_{DC} = 150 V, which

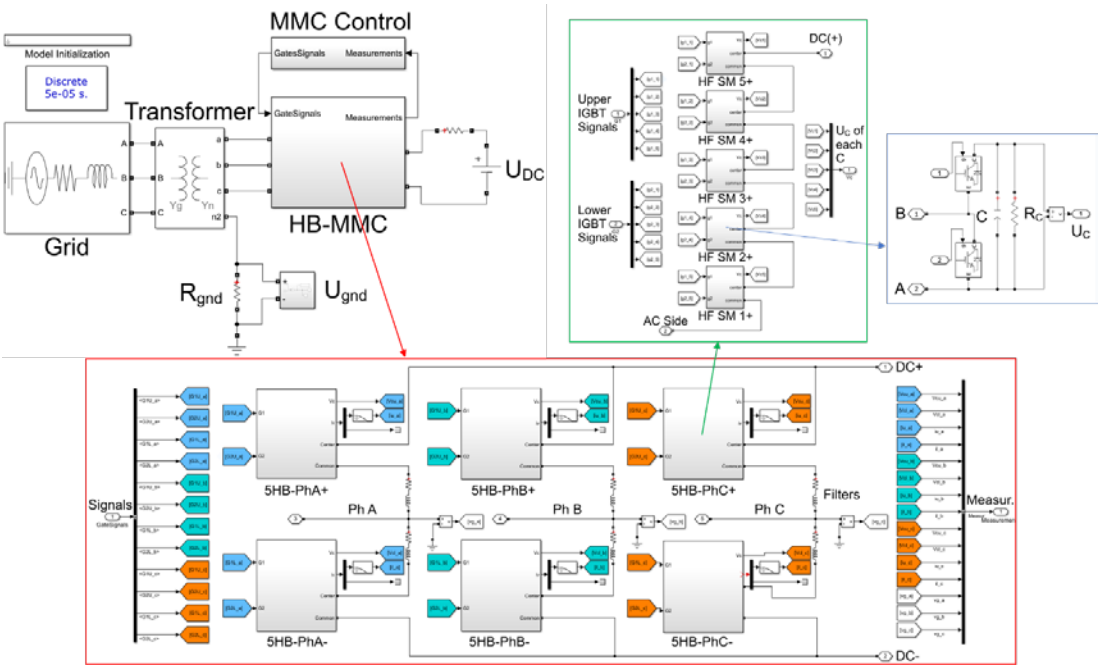

Fig. 6. Simulation setup with AC neutral grounding configuration [(up-left side of the picture): MMC general scheme; (red): MMC arms AC-DC connection; (green): 5 HF-SM of the upper part of phase C arm; (blue): HF-SM configuration].

TABLE I
SIMULATION SETUP PARAMETERS

Element	Parameter	Magnitude
AC Three Power Source	U_{AC}	120 V (ph-gnd)
Power Transformer	R_1	0.01613 Ω
	L_1	0.00205 H
	R_2	0.00250 Ω
	L_2	0.00032 H
	R_{Fe}	4032.3 Ω
	L_μ	12.835 H
	U_{1n}/U_{2n}	120/50 V/V
AC Filters	R_{filter}	0.1 Ω
	L_{filter}	0.008 H
SM Capacitors	C	3300 μF
	R_c	6000 Ω
DC side	U_{DC}	150 V_{DC}
	R_{DC}	0.1 Ω
Grounding elements	R_{gnd}	4700 Ω
	$R_1 = R_2$	4700 Ω

has been modeled as its Thevenin equivalent, U_{DC} = 150 V, R_{DC} = 0.1 Ω.

The AC side of the inverter has a power transformer with its neutral point accessible and where a R_{gnd} = 4.7 kΩ has been placed (see Fig. 6), however, some simulations have considered the DC midpoint grounding with $R_{gnd} = R_1 = R_2$ = 4.7 kΩ. This way, the maximum possible fault current is limited up to 16 mA. The simulation elements' characteristics can be seen in Table I.

In this simulation setup, the MMC works as an AC current source and its control is performed in two level current regulation loops according to [26], i.e., the grid current loop, that regulates the power flow of the MMC and the circulating current loop that manages the capacitors energy.

B. Healthy state simulations

Previously to the fault simulations, a healthy state one has been carried out. The results can be observed in Fig. 7, where

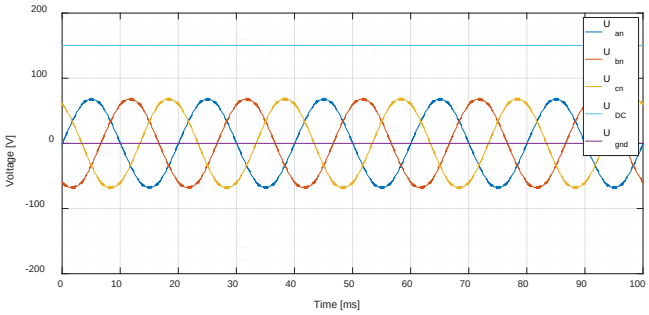

Fig. 7. Healthy simulation time domain voltage waveforms [U_{gnd} = 0 V].

the AC phase voltages, U_{an}, U_{bn} and U_{cn}, are balanced, U_{DC} has a value of 150 V_{DC}, and U_{gnd} has null value. It is because no fault current flues through R_{gnd}. Then, when the voltage measured in U_{gnd} will be lower than a certain threshold, the method will not actuate. A low threshold setting will be more sensitive to high impedance GFs, but an excessive low threshold could cause undesirable method's actuations.

C. AC Side GFs simulations

Once the healthy state method has been corroborated, some GFs have been simulated. First, AC side GFs were tested. In Fig. 5, an example of AC side GF for the phase "b" and R_f = 2.2 kΩ is plotted in time domain (Fig. 8.a) and in frequency domain (Fig. 8.b). As it is shown, phase in fault can be detected because U_{gnd} is in counterphase with the faulty phase voltage, in this case U_{bn}, which also experience a reduction in comparison with the healthy phases. Also, only f_1 component appears in the U_{gnd} frequency spectrum after performing a FFT.

D. DC side GFs simulations

For DC side GFs, only 0 Hz component appears in the FFT as well as commutation components. In Fig. 9, two GFs have been simulated. Fig. 9.a shows a fault in the DC(+) pole for R_f

= 2.2 kΩ, where Fig. 9.b shows a fault in the DC(-) pole for the same R_f. It can be clearly observed that the U_{gnd} polarity is inverse to the pole in fault. Finally, Fig. 9.c shows the FFT corresponding to the Fig. 9.a, where only U_{gnd} (f_0) is measured.

E. Submodules GFs simulations

Despite their lower probability, GFs in submodules can also appear. Fig. 10 shows an example of GF simulation in the SM3+ (or 80% of the arm) of the phase "a" with R_f = 2.2 kΩ. In Fig. 10.a, the fault can be discerned in the phase "a" as U_{gnd} is in counterphase with U_{an}, and also this phase-voltage has suffered a reduction in comparison with the healthy voltages. Then, in Fig. 10.b, after performing the FFT of U_{gnd} and U_{an}, an SM GF can be diagnosed as U_{gnd} (f_0) and U_{gnd}(f_1) appears. With both values and applying (1), the percentage of MMC arm where the fault is taking placed can be estimated.

Table II collects other simulation results with different fault resistances and other fault locations. In this table, fault position and R_f estimation is also provided for AC neutral and DC midpoint connections. Looking to Table II, it can be seen that the fault position estimation has good accuracy even for high fault resistances. The fault resistance will imply lower U_{gnd} measures and also lower U_{in} variations. This way, it is recommended to detect the AC phase in fault by observing the first harmonic angle difference between U_{in} and U_{gnd} instead for comparison among phase voltage modules as it will have better results for high impedance faults. Also, the accuracy in the R_f estimation for the AC connection is good enough. This R_f estimation loses accuracy when it is performed from the DC artificial midpoint (with R_1 = R_2 = 4.7 kΩ). Finally, it might be highlighted that R_f estimations have better results using eq. (24) or (25).

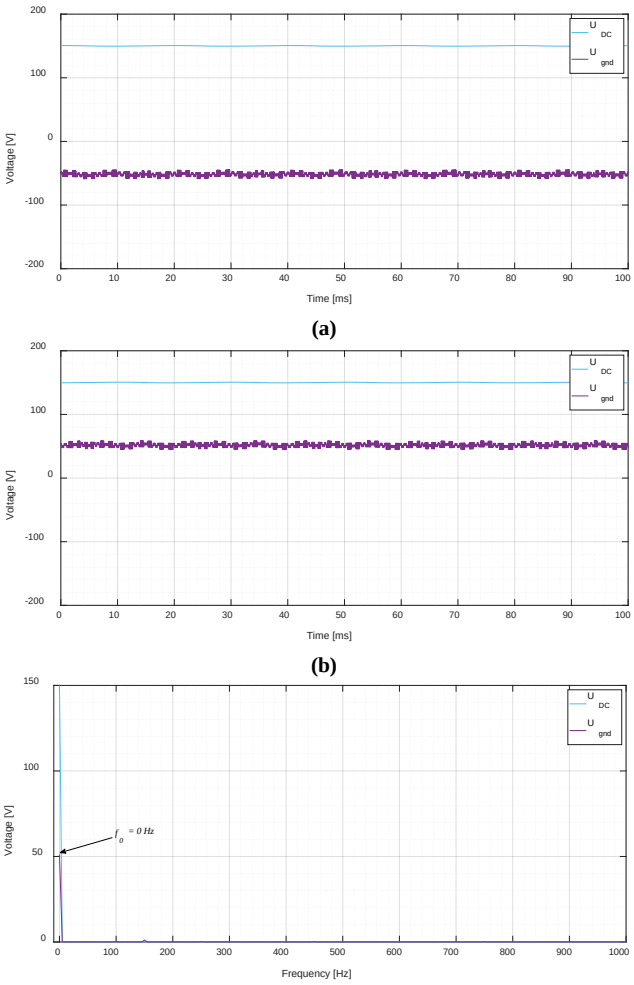

Fig. 9. GF in the DC side of the MMC, voltage measurements [R_f = 2.2 kΩ; (a): Fault in the DC(+) pole, time domain; (b): Fault in the DC(-) pole, time domain; (c): frequency domain for the DC(+) fault case].

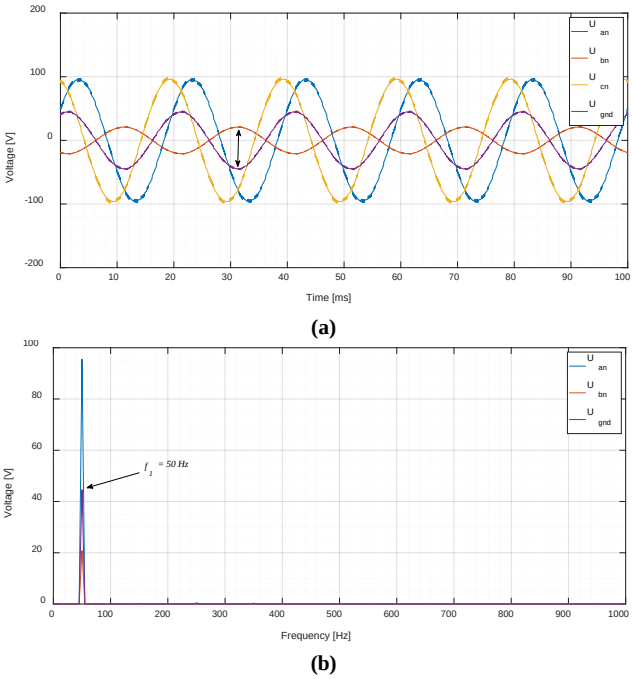

Fig. 8. GF in the AC side of the MMC [Faulty phase = "b"; R_f = 2.2 kΩ; (a): time domain voltage; (b): frequency domain voltage].

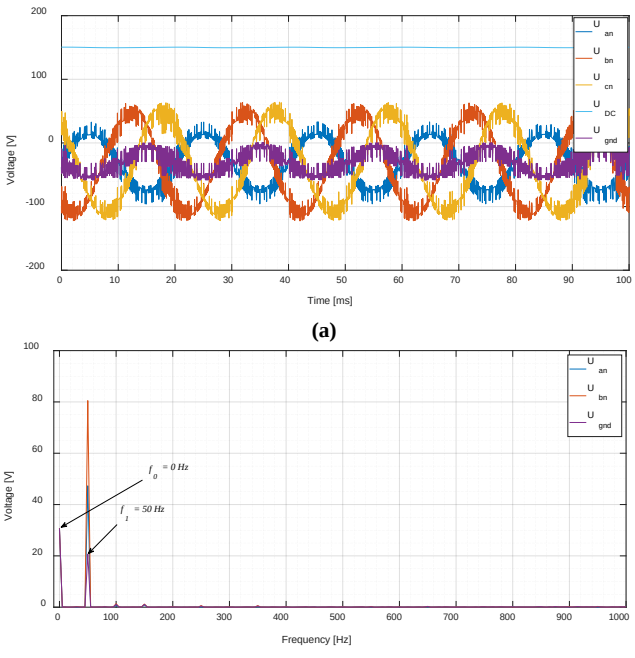

Fig. 10. GF in the SM3(+) of the MMC [Faulty phase = "a"; R_f = 2.2 kΩ; (a): time domain voltage; (b): frequency domain voltage].

TABLE II
SIMULATION RESULTS

Simulation (Fault position)		AC neutral point grounded R_{gnd} = 4.7 kΩ (Fault estimation)						DC artificial midpoint grounded $R_{gnd} = R_1 = R_2$ = 4.7 kΩ (Fault estimation)					
Position	R_f [kΩ]	U_{gnd} (0 Hz) [V]	U_{gnd} (50 Hz) [V]	U_{in} [V]	U_{DC} [V]	x [%]	R_f [kΩ]	U_{gnd} (0 Hz) [V]	U_{gnd} (50 Hz) [V]	U_{in} [V]	U_{DC} [V]	x [%]	R_f [kΩ]
0	2.2	51.19	0.112	67.99	150.01	0.11	2.171	38.10	0.2394	67.99	149.97	0.31	2.143
SM4─	2.2	40.96	10.30	57.61	150.01	10.1	2.177	30.47	7.818	56.25	149.98	10.2	2.158
SM3─	2.2	30.70	20.60	47.32	150.00	20.1	2.172	22.79	15.52	44.73	149.98	20.3	2.136
AC	2.2	0.001	44.61	20.88	147.66	50.0	2.500	0.871	28.71	23.71	149.31	48.5	5.035
SM1+	2.2	-10.23	40.69	27.24	150.00	60.1	2.223	-9.207	19.69	38.45	149.87	65.9	5.114
SM3+	2.2	-30.76	20.62	47.30	150.01	79.9	2.162	-22.79	15.51	44.70	149.98	79.8	2.167
DC(+)	2.2	-51.18	0.096	67.97	150.01	99.9	2.175	-38.10	0.239	67.94	149.97	99.7	2.145
SM3+	0	-46.70	28.55	37.94	149.54	81.0	0.030	-29.19	19.03	38.16	149.55	80.3	0.246
SM3+	4.7	-22.52	14.98	53.01	150.03	80.0	4.702	-17.99	12.10	49.92	150.02	79.9	4.669
SM3+	10	-14.40	9.504	58.52	150.06	80.1	10.05	-12.40	8.239	55.77	150.04	80.0	10.01

IV. EXPERIMENTAL TESTS

To additionally validate the proposed fault location method, experimental tests were carried out in a 60-kVA 12-levels FB three-phase MMC.

A. Experimental Setup

The experimental setup of the 60-kVA 12-levels FB three-phase MMC (1) can be seen in Fig. 11. The experimental setup consists of a MMC (1) fed from a 200 kVA – 50 Hz AC microgrid (2) following the electrical scheme of Fig. 1.b. The grid and the MMC are galvanically isolated through a main power transformer without neutral accessible.

During the tests, the operating AC and DC voltages were set to 120 V_{AC} and 300 V_{DC}, respectively. The MMC has its terminals for AC connections and DC positive and negative pole connections accessible (3). Additionally, the FB-SMs (4) have the terminals of their capacitors accessible for the three phases. A SM scheme in the upper-right side of Fig. 11 is shown. As examples, in the right side of Fig. 11, the lower arm SM terminals of phase "A" (5A) and "B" (5B) are shown.

In order to protect the entire system, three equal resistors, R = 5 kΩ, have been installed. They limit I_f up to 40 mA in the worst case. Two of them, $R_1 = R_2$, are utilized as an artificial DC midpoint grounding (6). The third one will be used as R_{gnd} (7). Also, five resistors of 2.2 kΩ (8) have been connected in series they will emulate different R_f. With a by-pass system (9), this fault resistance can be changed among the following values: 0, 2.2, 4.4, 6.6, 8.8 and 11 kΩ. If no by-pass is performed, R_f = 11 kΩ. On the other hand, attending to the number of by-passed resistors the R_f decreases up to 0 Ω in steps of 2.2 kΩ. The GFs were implemented (10) by connecting the R_f to a AC, DC or SM terminal of the MMC.

The MMC control is executed from a computer (12) utilizing OPAL-RT. With the OPAL-RT, U_{gnd} is measured utilizing a voltage transductor (11) and collecting the measurement in real time with the rest of telemetry in the computer (12). From this telemetry, the measurements of U_{an}, U_{bn}, U_{cn} and U_{DC} have been collected to carry out the method with a sample frequency of 10 kHz and with a record time length of 200 ms.

B. Healthy state test

A healthy condition test was conducted in order to corroborate that U_{gnd} is close to 0 V and to calibrate the measurements, regarding to the DC component. The healthy state test can be seen in Fig. 12. The MMC main parameters were U_{DC} = 300 V, U_{in} = 120 V and i_d = 10 A. Furthermore, the voltage of each arm was set to 300 V_{dc}, thus, U_{SMj} = 25 V each. The voltage in each SM capacitor was

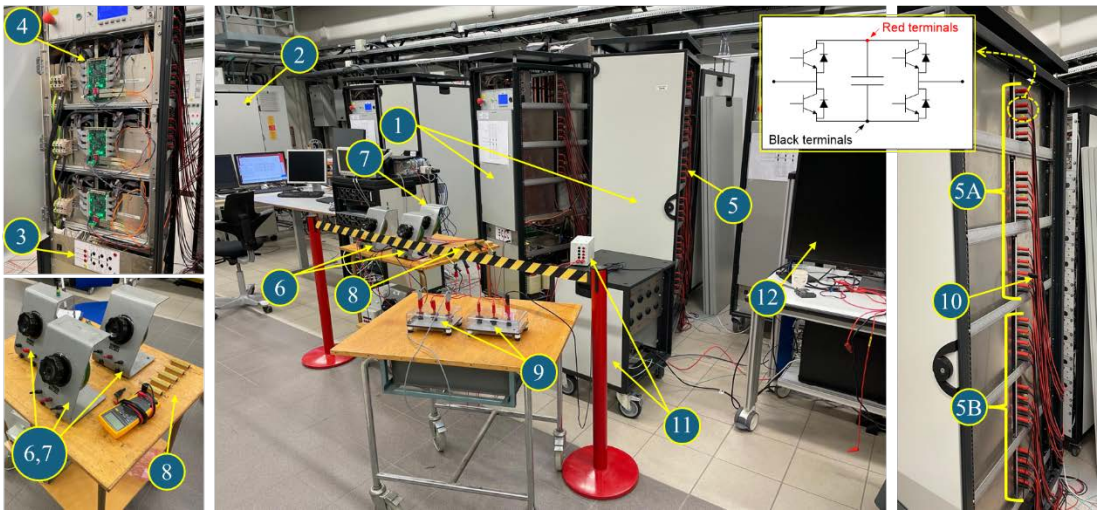

Fig. 11. Experimental setup [(1): 60-kVA 12-levels FB three-phase MMC; (2): 200 kVA microgrid; (3): AC and DC side connections of the MMC; (4): FB-SM; (5): SM terminals; (6): Artificial DC midpoint; (7): Grounding resistor; (8): Fault resistors; (9): Fault resistance selector; (10) GF connection; (11): Voltage

transducer; (12): Computer].

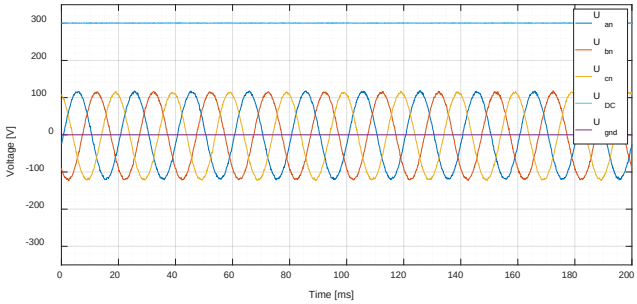

Fig. 12. Healthy state experimental test [U_{DC} = 300 Vdc, U_{in} = 120 V_{peak}; AC current in "d" axis = 10 A].

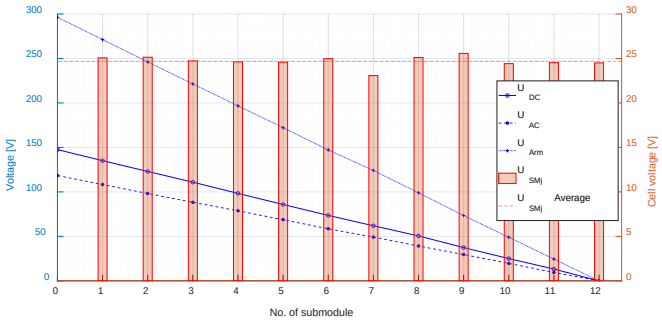

Fig. 13. U_{AC}, U_{DC}, U_{arm} and U_{SMj} distributions along the lower arm of the phase "a" in the MMC measured from the DC(-) pole.

measured to ensure the linear behavior of the MMC arms (see Fig. 13). In the worst case, U_{SMj} differences up to 2.04V were noticed, i.e., less than 8.1% of the U_{SMj} average value.

C. AC Side GFs tests

Numerous GFs were performed in the AC terminals of the MMC (x = 50 %). Considered faults were R_f = [0, 2.2, 4.4, … 11] kΩ for the three phases, which are a total of 18 tests.

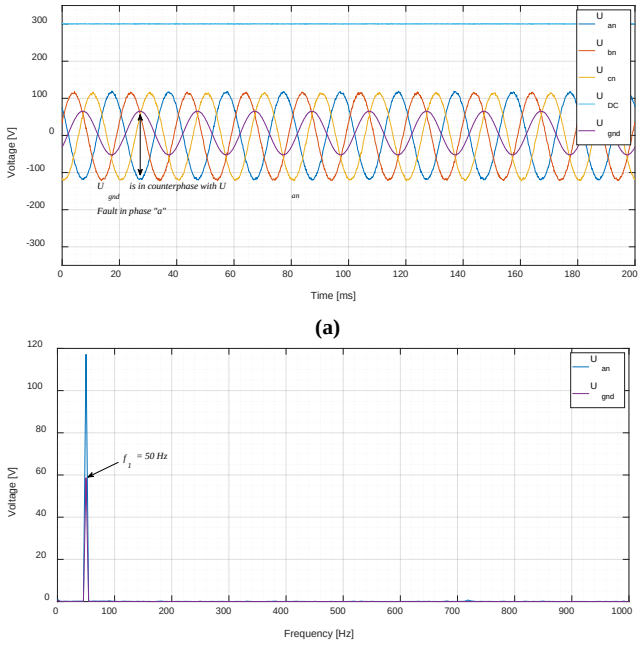

(a) **(b)**

Fig. 14. GF experimental test in the AC side of the MMC [Faulty phase = "a"; R_f = 2.2 kΩ; (a): time domain voltage; (b): frequency domain voltage].

A fault in the phase "a" with R_f = 2.2 kΩ is shown as example of this type of faults in Fig. 14. As it can be seen, U_{gnd} is in counterphase with U_{an}, which allows discerning the faulty phase. Additionally, from Fig. 14.b it can be known that the fault is in x = 50 % as no $U_{gnd}(f_0)$ appears.

It must be highlighted, that U_{an} does not suffer attenuation, as the U_{in} voltage measurements are the phase-to-neutral voltage but not phase-to-ground voltages of the main power transformer. However, the measurements are also valid for the fault location.

D. DC side GFs tests

In order to validate the DC (-) and DC (+) pole faults (x = 1 and 0, respectively), faults with R_f = [0, 2.2, 4.4, … 11] kΩ were tested. A set of 12 faults was performed to analyze this event.

Fig. 15 shows two different GFs considered in the experimental tests. One of the faults of the figure was performed in the DC (+) pole with R_f = 2.2 kΩ. When this fault was performed, the $U_{gnd}(f_1)$ component was not measured. By contrast, $U_{gnd}(f_0)$ component appears (see Fig. 15.b). The polarity of $U_{gnd}(f_0)$ suggests that the fault is in the DC(+) fault as it happened in simulations and previously suggested in the methodology. The voltage of this fault reaches $U_{gnd}(f_0)$ = -75 V. The other fault corresponds with a fault in the DC (-) pole with R_f = 0 kΩ. This fault has opposite polarity to the pole in fault as well and a higher magnitude in $U_{gnd}(f_0)$, which reaches up to 100 V. The difference between both magnitudes is due to the voltage drop in R_f, which is negligible for the second case.

E. Submodules GFs tests

Finally, 864 fault tests in the SM of the MMC were performed. These tests were carried out for R_f = [0, 2.2, 4.4, … 11] kΩ in the black and red terminals of the SM connections,

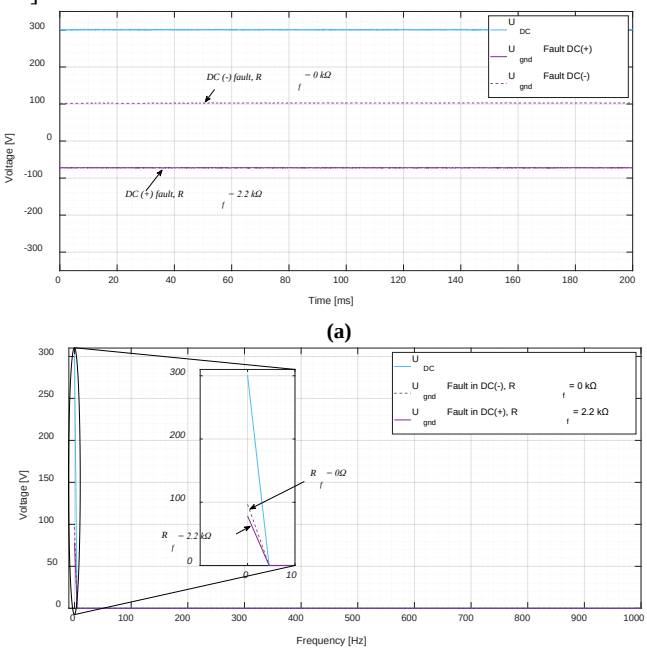

(a) **(b)**

Fig. 15. GF experimental tests in the DC side of the MMC, voltage measurements [(a): A fault in the DC(+) pole, R_f = 2.2 kΩ, and a fault in the DC(-) pole, R_f = 0 kΩ, time domain; (b): both faults in frequency domain].

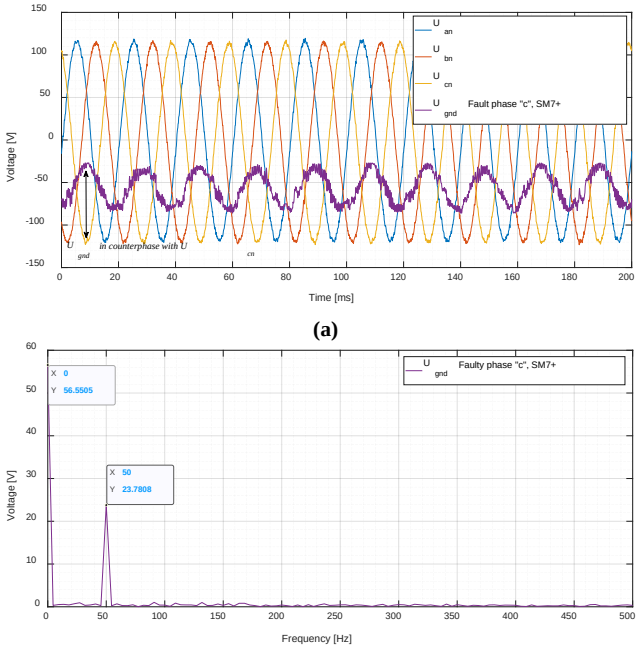

Fig. 16. GF experimental test in the SM7+ of the MMC [Faulty phase = "c"; R_f = 2.2 kΩ; (a): time domain voltage; (b): frequency domain voltage].

of the 24 SM per phase (12 for the upper arm and 12 for the lower arm) for the three phases of the system. An additional group of 6 tests varying the operating conditions of U_{DC} [300, 330, 360 V] and U_{AC} [75, 100, 120 V] have been also included. These parameters have not significantly affected the location results.

One example is shown in Fig. 16. The example case corresponds to a fault with R_f = 2.2 kΩ in the SM7+ of the phase "c". It can be seen that in Fig. 16.a, U_{gnd} is in counterphase with U_{cn}, also it has DC negative component, which implies that the fault is in the DC(+) pole. As it is an hybrid case, it implies that the fault is concatenated inside the upper arm of the phase "c". From Fig. 16.b, both $U_{gnd}(f_0)$ and $U_{gnd}(f_1)$ appear. Introducing both values in the location equation (21) considering the sign of $U_{gnd}(f_0)$ as negative, the

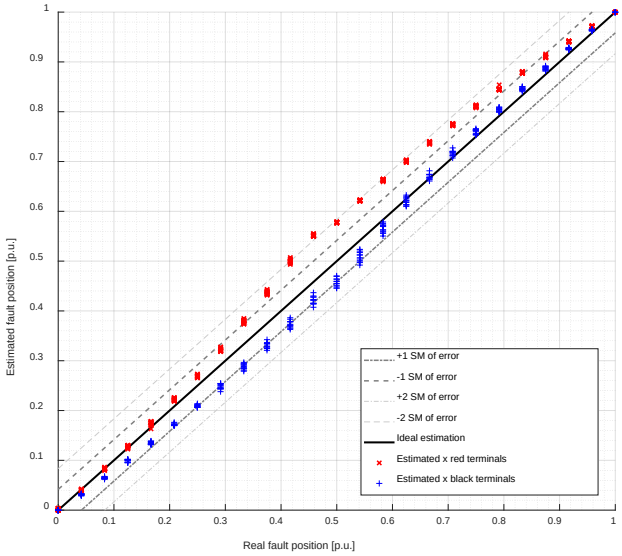

Fig. 17. Experimental fault location estimations for all the fault positions in the SM of the MMC.

fault position is estimated as x = 85.2 %. It implies that the SM8+ is estimated as the faulty SM. However, the real location that corresponds with SM7+ is x = 79.16%.

In Fig. 17, the 864 fault cases for GFs in the SMs are plotted distinguishing between red and black terminals faults. In this figure, the real fault location is in the X-axis, while the estimated x is plotted in the Y-axis. In an ideal case, the line $x_{real} = x_{estimated}$ should be given. In this figure, the ideal location and the deviations of ±1 and ±2 SMs are also plotted. On the one hand, from the figure, the set of tests performed at the red terminals of each SM for the different R_f are prone to have excess errors up to +2 SM. On the other hand, the black terminal GF locations have deficiency errors up to -1 SM. Despite this, the dispersion provoked by R_f is almost negligible, as it can be seen that all the points follow a narrow and defined progression from x = 0 to x = 1. An example of numerical results is plotted in Table III, where the results of x estimation, deviation error and R_f estimation of the black terminals of the phase "a" are plotted for all the R_f.

TABLE III
EXPERIMENTAL RESULTS: BLACK TERMINAL POSITIONS IN PHASE "A"

X_{real}	x_{real} [%]	$x_{estimated}$ [%]						SM deviation						R_f estimated [kΩ]					
		R_f = 0 kΩ	R_f = 2.2 kΩ	R_f = 4.4 kΩ	R_f = 6.6 kΩ	R_f = 8.8 kΩ	R_f = 11 kΩ	R_f = 0 kΩ	R_f = 2.2 kΩ	R_f = 4.4 kΩ	R_f = 6.6 kΩ	R_f = 8.8 kΩ	R_f = 11 kΩ	R_f = 0 kΩ	R_f = 2.2 kΩ	R_f = 4.4 kΩ	R_f = 6.6 kΩ	R_f = 8.8 kΩ	R_f = 11 kΩ
DC(+)/ SM12+	100.00	100.00	99.99	99.99	100.00	100.00	100.00	0	0	0	0	0	0	0.01	2.20	4.32	6.39	8.65	10.31
SM11+	95.83	96.31	96.28	96.61	96.34	96.54	96.40	0	0	0	0	0	0	0.62	3.23	5.84	8.50	11.29	14.11
SM9+	87.50	88.85	89.02	88.97	88.77	88.52	88.19	0	0	0	0	0	0	0.95	3.64	6.41	9.28	12.13	15.04
SM7+	79.17	80.25	80.92	80.57	80.20	80.14	79.96	0	0	0	0	0	0	1.31	4.16	7.02	10.02	13.05	16.07
SM5+	70.83	71.71	71.92	71.98	71.70	71.46	71.16	0	0	0	0	0	0	1.73	4.75	7.82	10.93	14.17	17.35
SM3+	62.50	61.79	62.73	62.17	61.93	61.39	61.12	0	0	0	0	0	0	2.20	5.36	8.64	11.94	15.37	18.79
SM1+	54.17	50.24	51.88	51.27	50.70	50.10	49.72	-1	-1	-1	-1	-1	-1	2.71	6.01	9.46	12.95	16.56	19.85
AC	50.00	45.38	46.37	45.91	45.51	45.05	44.64	-1	-1	-1	-1	-1	-1	1.73	4.40	7.07	9.73	12.31	14.84
SM1-	45.83	42.12	42.85	42.31	42.21	41.51	41.40	-1	-1	-1	-1	-1	-1	1.79	4.47	7.11	9.80	12.35	14.97
SM3-	37.50	33.07	33.66	33.42	32.92	32.55	32.54	-1	-1	-1	-1	-1	-1	1.43	4.03	6.60	9.13	11.62	14.19
SM5-	29.17	24.61	25.26	25.01	24.67	24.38	24.94	-1	-1	-1	-1	-1	-1	1.02	3.53	6.00	8.43	10.80	13.28
SM7-	20.83	17.08	17.29	17.05	17.14	17.28	16.99	-1	-1	-1	-1	-1	-1	0.76	3.11	5.53	7.90	10.21	12.46

SM9-	12.50	9.93	10.17	10.02	10.07	10.17	9.52	-1	-1	-1	-1	-1	-1	0.42	2.77	5.08	7.36	9.65	11.77
SM11-	4.17	3.24	3.30	3.21	3.23	3.11	3.11	0	0	0	0	0	0	0.17	2.44	4.70	6.90	9.05	11.14
SM12-/ DC (-)	0.00	0.02	0.02	0.00	0.00	0.00	0.00	0	0	0	0	0	0	0.03	2.26	4.47	6.68	8.83	10.82

From the results collected in Table III, the maximum location error is reached in the higher R_f and close to x = 50 %. The maximum error observed is 5.36% in x = 50 % and R_f = 11 kΩ, which implies a deviation of one SM and an additional error of 1.20 %. In the middle of Table III, the deviation of SM estimation can be observed. The bigger errors are reached in the lower arm x estimations. Finally, in terms of R_f estimation, the accuracy of the estimation decreases from the DC(+) and DC(-) to the AC side. The closer is the fault to the AC side, the higher is the estimation error.

V. Discussion of the Results

From the experimental and simulation results, different observations can be performed.

The first one is related to the fault position, x, estimation. GFs in the simulations were perfectly observed since no problems with resolutions and measurement accuracies exist. However, in experimental tests, some deviations have been observed around x = 50 % when the GFs have been done in the SM. This fact is due to the resolution of the $U_{gnd}(f_0)$ measurement when the fault is close to the AC side, which value directly affects eq. (21). However, this problem does not affect faults directly performed in the AC side, where $U_{gnd}(f_0)$ is 0 V.

The second observation comprises the location error committed in the experimental tests, which varies between +2 SM and -1 SM. The fact of having an error of an entire SM of difference is due to the switching position of the SM, which can vary one the real GF position a 4.16% in case of the experimental tests, i.e., 1 out of 24 SMs. In Fig. 18, the errors are recalculated attending to the two possible positions of each SM, the direct or reverse feeding of the SM (see Fig. 19.a and Fig. 19.b respectively). It implies that a systematic error of 4.16% is delimit between both possibilities and it can be taken as uncertainty in the GF position estimation.

Another appointment must be done around the R_f estimation. From the experimental results, the severity estimation becomes less accurate as it is farther from the DC(+) and DC(-) poles. However, also appears in the simulation results, where the severity of the GFs near the AC side are not well estimated. Facts like the DC midpoint displacement in the event of a fault, the low circulating currents through R_1, R_2 and R_{gnd} and the already existing x estimation error add error to the R_f estimation. For this reason, the use of direct DC midpoints (see Fig. 2) or AC neutral groundings through R_{gnd} (see Fig. 1.a) is strongly recommended instead of using artificial DC midpoints (see Fig. 1.b).

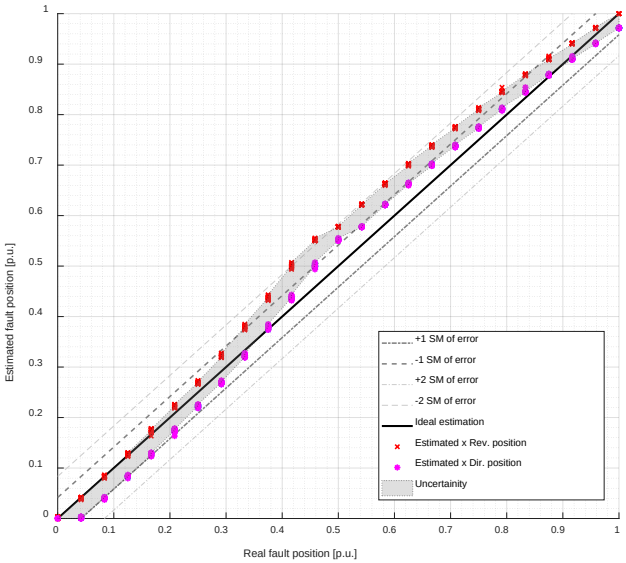

Fig. 18. Uncertainty error caused due to the fault position variation inside the SM [Red terminals case study].

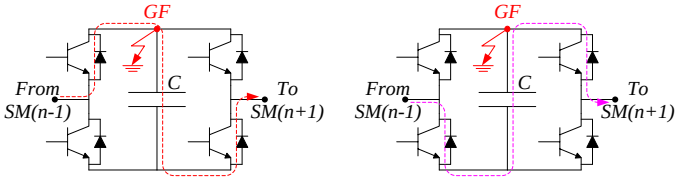

(a) **(b)**

Fig. 19. SM feeding [(a): direct feeding; (b): reverse feeding].

Despite the location errors, the ground fault location method allows to easily estimate the faulty phase and with an admissible accuracy the SM in fault. This will save a lot of time during the MMC maintenance. Furthermore, the fault estimation can give an approximation about the severity of the defect and the urgency of the maintenance.

VI. Conclusions

The use of MMCs is becoming a significant technology in power systems as for example in HVDC systems. However, the use of many power-electronic elements makes difficult their GF diagnosis.

This paper proposed a GF location method based on AC neutral or DC midpoint high resistance grounding for the fault location. Measuring the grounding resistor voltage, U_{gnd}, the AC phase voltages and DC total voltage the fault location can be totally discerned. The fault will be in the AC side if U_{gnd}

has only fundamental frequency component, and analogously for the DC side. A combination of AC and DC components will only appear in U_{gnd} when the fault is taking place in a SM. Comparing this voltage with the phase voltages, the faulty AC phase, or the voltage polarity the faulty DC pole, is discerned.

The method has been validated through simulations in a HB 5-levels three-phase MMC achieving accurate results in the position and severity estimation. It has been also validated though experiments in a 60 kVA FB 12-levels three-phase MMC reaching location errors comprised between (-1 SM, +2 SM). Despite the severity estimation has presented more inaccuracies than in simulations, the results have proven that the diagnosis made by the method is suitable for saving a lot of time during the maintenance of the equipment.

However, this investigation lead the doors open to further works that should be focus on the experimental validation of the method utilizing an AC neutral grounding configuration and in the design of a fault tolerant control taking the information of the diagnosis method into account.

REFERENCES

[1] J. -Y. Wu, S. Lan, S. -J. Xiao and Y. -B. Yuan, "Single Pole-to-Ground Fault Location System for MMC-HVDC Transmission Lines Based on Active Pulse and CEEMDAN," in *IEEE Access*, vol. 9, pp. 42226-42235, 2021.

[2] Y. Ma, J. Xiao, H. Lin and Z. Wang, "A Novel Battery Integration Method of Modular Multilevel Converter with Battery Energy Storage System for Capacitor Voltage Ripple Reduction," in *IEEE Transactions on Industrial Electronics*, vol. 68, no. 12, pp. 12250-12261, Dec. 2021.

[3] J. H. D. G. Pinto, W. C. S. Amorim, A. F. Cupertino, H. A. Pereira, S. I. S. Junior and R. Teodorescu, "Optimum Design of MMC-Based ES-STATCOM Systems: The Role of the Submodule Reference Voltage," in *IEEE Transactions on Industry Applications*, vol. 57, no. 3, pp. 3064-3076, May-June 2021.

[4] S. Wu *et al*., "A Modular Multilevel Converter with Integrated Energy Dissipation Equipment for Offshore Wind VSC-HVDC System," in *IEEE Transactions on Sustainable Energy*, vol. 13, no. 1, pp. 353-362, Jan. 2022.

[5] F. Deng, Y. Lü, C. Liu, Q. Heng, Q. Yu and J. Zhao, "Overview on submodule topologies, modeling, modulation, control schemes, fault diagnosis, and tolerant control strategies of modular multilevel converters," in *Chinese Journal of Electrical Engineering*, vol. 6, no. 1, pp. 1-21, March 2020.

[6] Y. Tao, L. Zhang, C. Wang and K. Yu, "A Fault Location Strategy for IGBT Open-Circuit Fault in Modular Mutilevel Converter," *2020 12th IEEE PES Asia-Pacific Power and Energy Engineering Conference (APPEEC)*, 2020, pp. 1-5.

[7] T. Gruhn, J. Glenney and M. Savostianik, "Type B Ground-Fault Protection on Adjustable Frequency Drives," in *IEEE Transactions on Industry Applications*, vol. 54, no. 1, pp. 934-939, Jan.-Feb. 2018.

[8] U. Snahzad, S. Kahrobaee, S. Asgarpoor, "Protection of Distributed Generation: Challenges and Solutions," *in Energy and Power Engineering*, vol. 9, no.10, pp. 614-653, 2017.

[9] J. M. Guerrero, G. Navarro, K. Mahtani and C. A. Platero, "Ground Fault Detection Method for Variable Speed Drives," in *IEEE Transactions on Industry Applications*, vol. 57, no. 3, pp. 2547-2558, May-June 2021.

[10] F. R. Blánquez, C. A. Platero, E. Rebollo and F. Blázquez, "Novel Rotor Ground-Fault Detection Algorithm for Synchronous Machines With Static Excitation Based on Third-Harmonic Voltage-Phasor Comparison," in *IEEE Transactions on Industrial Electronics*, vol. 63, no. 4, pp. 2548-2558, April 2016.

[11] L. Xu *et al*., "A Review of DC Shipboard Microgrids—Part II: Control Architectures, Stability Analysis, and Protection Schemes," in *IEEE Transactions on Power Electronics*, vol. 37, no. 4, pp. 4105-4120, April 2022.

[12] S. Ansari, H. Samet and T. Ghanbari, "Fault Location in Solar Farms," in *IEEE Systems Journal*, vol. 15, no. 3, pp. 4003-4012, Sept. 2021.

[13] G. Song, J. Hou, B. Guo, T. Wang, B. Masood, S. T. Hussain Kazmi," Single-ended active injection for fault location in hybrid MMC-HVDC systems," *International Journal of Electrical Power & Energy Systems*, Volume 124, 2021.

[14] J. He, Q. Yang and Z. Wang, "On-line fault diagnosis and fault-tolerant operation of modular multilevel converters — A comprehensive review," in *CES Transactions on Electrical Machines and Systems*, vol. 4, no. 4, pp. 360-372, Dec. 2020.

[15] X. Shi, Z. Wang, B. Liu, Y. Liu, L. M. Tolbert and F. Wang, "Characteristic Investigation and Control of a Modular Multilevel Converter-Based HVDC System Under Single-Line-to-Ground Fault Conditions," in *IEEE Transactions on Power Electronics*, vol. 30, no. 1, pp. 408-421, Jan. 2015.

[16] H. Aji, M. Ndreko, M. Popov and M. A. M. M. van der Meijden, "Investigation on different negative sequence current control options for MMC-HVDC during single line to ground AC faults," *2016 IEEE PES Innovative Smart Grid Technologies Conference Europe (ISGT-Europe)*, Ljubljana, Slovenia, 2016, pp. 1-6.

[17] S. Ma, J. Xu, G. Wu, Y. Wang, Y. Song, G. Yu, and Z. Liu, "Characteristic investigation of MMC-HVDC system under internal AC bus fault conditions," in *The Journal of Engineering*, pp. 2228-2232, 2019.

[18] G. Li, J. Liang, C. E. Ugalde-Loo, F. Ma, H. Liang and Z. Song, "Protection for Submodule Overvoltage Caused by Converter Valve-Side Single-Phase-to-Ground Faults in FB-MMC Based Bipolar HVDC Systems," in *IEEE Transactions on Power Delivery*, vol. 35, no. 6, pp. 2641-2650, Dec. 2020.

[19] W. Liu, G. Li, J. Liang, C. E. Ugalde-Loo, C. Li and X. Guillaud, "Protection of Single-Phase Fault at the Transformer Valve Side of FB-MMC-Based Bipolar HVdc Systems," in *IEEE Transactions on Industrial Electronics*, vol. 67, no. 10, pp. 8416-8427, Oct. 2020.

[20] J. M. Guerrero, G. Navarro, C. A. Platero, P. Tian and F. Blázquez, "A Novel Ground Fault Detection Method for Electric Vehicle Powertrains Based on a Grounding Resistor Voltage Analysis," in *IEEE Transactions on Industry Applications*, vol. 56, no. 5, pp. 4934-4944, Sept.-Oct. 2020.

[21] J. M. Guerrero, M. J. Carrizosa, K. Mahtani and C. A. Platero, "A Ground Fault Location Method for Modular Multilevel Converters," *2023 IEEE 14th International Symposium on Diagnostics for Electrical Machines, Power Electronics and Drives (SDEMPED)*, Chania, Greece, 2023, pp. 297-302.

[22] J. M. Guerrero and M. Jiménez-Carrizosa, "System and Method of ground fault localization in a direct current and altern current electric installation with modular multilevel converter," Spanish Patent no. ES2934620B2 (31.10.2022), Oficina Española de Patentes y Marcas, Madrid.

[23] J. M. Guerrero, G. Navarro, K. Mahtani and C. A. Platero, "AC Drive Side Ground Fault Location for DC/AC Systems Based on AC Phases and Grounding Resistor Voltages," in *IEEE Transactions on Industry Applications*, vol. 58, no. 3, pp. 3567-3577, May-June 2022.

[24] F. Deng and Z. Chen, "Voltage-Balancing Method for Modular Multilevel Converters Switched at Grid Frequency," in *IEEE Transactions on Industrial Electronics*, vol. 62, no. 5, pp. 2835-2847, May 2015.

[25] L.A.M. Barros, A.P. Martins, J.G. Pinto, "A Comprehensive Review on Modular Multilevel Converters, Submodule Topologies, and Modulation Techniques," *in Energies*, vol. *15*, 1078, 2022.

[26] N. Stanković, M. J. Jiménez Carrizosa, A. Arzandé, P. Egrot and J. -C. Vannier, "An HVDC experimental platform with MMC and two-level VSC in the back-to-back configuration," *2016 IEEE 25th International Symposium on Industrial Electronics (ISIE)*, Santa Clara, CA, USA, 2016, pp. 436-441.

AUTHORS' BIOGRAPHIES

Jose Manuel Guerrero (M'23) was born in Madrid, Spain, in 1996. He received the B.E. in energy resources, fuels and explosive engineering, the M.E. in electrical engineering and the Ph.D. degree in Electrical Engineering from the Universidad Politécnica of Madrid, Madrid, Spain, in 2018, 2019, and 2022 respectively.

He worked as Assistant Professor at the Department of Energy and Fuels at the Universidad Politécnica of Madrid from 2020 to 2023. In 2023, he was professor

and lecturer at the Electronics and Computing Department of Mondragon Unibertsitatea. Nowadays, he works in the Electrical Department of the Universidad del País Vasco as a Researcher Associate Professor where his research field is focused on electric systems protection and fault diagnosis.

Aitor Blázquez Campanón was born in Bilbao, Spain, in 1997. He received the B.E. in renewable energy engineering, the M.E. in integration of renewable energies in the electrical system from the Universidad del Pais Vasco (UPV), Bilbao, Spain, in 2020 and 2021 respectively. Nowadays, he is conducting his doctoral studies at the same organization.

He worked as an electrical engineer for Ingeteam from 2020 to 2022. In 2023, he started working for the Electrical Department of the Universidad del País Vasco, as a researcher where his research field is focused on the modeling of DC and AC electrical fault systems.

Salvatore D'Arco received the M.Sc. and Ph.D. degrees in electrical engineering from the University of Naples Federico II, Naples, Italy, in 2002 and 2005, respectively. From 2006 to 2007, he was a Postdoctoral Researcher with the University of South Carolina, Columbia, SC, USA.

In 2008, he joined ASML, Veldhoven, The Netherlands, as a Power Electronics Designer consultant, where he worked until 2010. From 2010 to 2012, he was a Postdoctoral Researcher with the Department of Electric Power Engineering, Norwegian University of Science and Technology, Trondheim, Norway. In 2012, he joined SINTEF Energy Research, Trondheim, where he is currently a Chief Research Scientist. He is the author of more than 130 scientific papers and a also holder of one patent. His main research interests include control and analysis of power-electronic conversion systems for power system applications, including real-time simulation and rapid prototyping of converter control systems.

Miguel Jiménez Carrizosa received the M.S. industrial engineering degree in electrical engineering from the Universidad Politecnica de Madrid (UPM), Madrid, Spain, in 2011, the M.S. degree in energy systems from Supélec, Gif-sur-Yvette, France, in 2011, and the Ph.D. degree in electrical engineering and automatic control from Paris-Sud XI University, Orsay, France, in 2015.

He is currently an Associate Professor with the Departamento de Energía y Combustibles, Escuela Técnica Superior de Ingenieros de Minas y Energía, UPM, and a Researcher with the Centro de Electrénica Industrial (CEI-UPM). His research interests include HVdc systems, control of power converters, transmission and distribution systems, integration of renewable energies, smart grids, and optimal power flow methods

Kumar Mahtani was born in 1997 in Tenerife (Spain). He obtained his BSc. and MSc. in Engineering with specialization in Electrical Engineering from Universidad Politécnica de Madrid, Spain, and CentraleSupélec (France), in 2020. After, he obtained his Ph.D. in Electrical Engineering from Universidad Politécnica de Madrid in 2023.

Since 2020, he works as Assistant Professor at the Electrical Engineering Department of Universidad Politécnica de Madrid.

Carlos A. Platero (M'10), (SM'20) was born in in Madrid, Spain, in 1972. He obtained the Dipl. degree and Ph.D. degree in Electrical Engineering from the Universidad Politécnica de Madrid, Spain, in 1996 and 2007 respectively.

From 1996 to 2008 he worked in ABB Generación S.A., Alstom Power S.A. and ENDESA Generación S.A., always involved in the design and commissioning of power plants.

In 2002 he began teaching at the Electrical Engineering Department of the Universidad Politécnica de Madrid and joined an energy research group. In 2022 he became a full Professor.